Wiley
International Journal of Energy Research
Volume 2024, Article ID 5586423, 14 pages
https://doi.org/10.1155/2024/5586423

WILEY

Research Article

Electrocatalytic Barrier Comprising Polar SnO_2 Quantum Dots Anchored Within Porous Carbon Microspheres Prepared by Spray Drying Process for Li–S Batteries

Kun Woo Baek,[1] **Geon Hui Oh**,[1] **Rakesh Saroha**,[1] **Dong-Won Kang**,[2] **Gi Dae Park**,[3] **and Jung Sang Cho**[1,4,5]

[1]*Department of Engineering Chemistry, Chungbuk National University, Cheongju 361-763, Chungbuk, Republic of Korea*
[2]*Department of Energy Systems Engineering, Chung-Ang University, Seoul 06974, Republic of Korea*
[3]*Department of Advanced Materials Engineering, Chungbuk National University, Cheongju 361-763, Chungbuk, Republic of Korea*
[4]*Biomedical Research Institute, Chungbuk National University Hospital, Cheongju 28644, Chungbuk, Republic of Korea*
[5]*Advanced Energy Research Institute, Chungbuk National University, Cheongju 28644, Chungbuk, Republic of Korea*

Correspondence should be addressed to Dong-Won Kang; kangdwn@cau.ac.kr and Jung Sang Cho; jscho@cbnu.ac.kr

Received 4 October 2023; Revised 29 August 2024; Accepted 28 September 2024

Academic Editor: Fatemeh Boshagh

Hypothesis: Porous carbon microspheres (PCMs) with embedded tin di-oxide (SnO_2) quantum dots (QDs) (P-SnO_2@PCMs) are synthesized and employed as polysulfide barriers to enrich the electrochemical properties.
Experiments: This composite structure is prepared by spray drying procedure and followed by heat-treatment, resulting in well-arranged macropores with a diameter of 59 nm generated by the polystyrene (PS) nanobeads ($\phi = 150$ nm) decomposition. P-SnO_2@PCMs is functioned as an electrocatalytic interlayer and offer advantages such as reduced diffusion length for charged particles that guarantees immediate transfer, improved electrode wetting due to efficient electrolyte infiltration, and accommodation of large volume fluctuations during the redox reactions. Furthermore, the incorporation of polar SnO_2 QDs within the microspheres allows for efficient chemical confinement and alteration of trapped polysulfide species due to catalytic activity, leading to an extensive use of the active material.
Findings: Advancing from the nanostructural eminence, lithium–sulfur (Li–S) cells paired with P-SnO_2@PCMs-coated separator and conventional sulfur electrode showed outstanding rate performance (321 mA h g^{-1} at 2.0 C) and prolonged cyclic steadiness at 0.1 C. This innovative synthesis strategy provides valuable insights for developing novel nanostructures applicable to various rechargeable devices.

Keywords: carbon framework; composite structure; functional interlayers; metal oxides; redox kinetics

1. Introduction

Over the past few years, lithium–sulfur (Li–S) battery (LSB) technology has captured considerable global interest, primarily owing to its remarkable theoretical capacity (1675 mA h g^{-1}) and superior energy density (2600 Wh kg^{-1}). The capacity of LSBs is nearly 10 times more than typical cathodes ($LiCoO_2$ and $LiFePO_4$) used in lithium–ion (Li–ion) batteries (LIBs) [1, 2]. Moreover, the abundant availability, eco-friendliness, and cost-effectiveness of sulfur (S) make LSBs a promising alternative to LIBs. As a result, LSBs emerge as a strong competitor for the next-generation batteries, capable of meeting the growing energy demands of the electronics industry. However, significant challenges impede the commercialization of LSBs, including rapid capacity decay, incomplete utilization of active sulfur (S), and poor Coulombic efficiency [3]. These drawbacks are mainly attributed to the substantial volume change of the electrodes and lithium polysulfide (LiPS) dissolution [4], as well as the minimal electrical conductivity of S and their final redox products (Li_2S/Li_2S_2) [5]. This study aims to address these critical challenges by developing a novel multifunctional interlayer that improves the electrochemical performance and mitigates the

issues related to polysulfide shuttling. By focusing on integrating polar materials within porous carbon microspheres (PCMs), this work introduces a proficient tactic to enhance the stability and efficiency of LSBs.

A promising approach to boost the electrochemical properties is to confine S within the porous and conductive matrices, creating a space for the formation of an adsorption barrier layer for LiPS and accommodating the volume expansion of active materials [6–8]. Therefore, it is essential to restrict the movement of dissolved LiPS intermediates during battery operation. Till now, various techniques have been explored to address the diffusion of LiPS [9, 10]. Moreover, the utilization of a barrier or interlayer between the separator and cathode was found effective in trapping the LiPS species [11]. For example, Su and Manthiram [12] revealed that a simple alteration of the LSBs configuration, such as incorporating a microporous bifunctional carbon paper between the separator and cathode, can enhance the usage of active material and improve capacity retention. The inception of carbon interlayer restricts the mobility of soluble LiPS species and reduces the internal resistance during charge transfer [13]. Besides, the attachment of additional layers composed of various carbonaceous material serves as physical barriers, efficiently suppress the diffusion of LiPS while maintaining a controlled rate of Li^+ transfer [14–16].

Carbonaceous materials usually exhibit initial capacity increments over several hundred cycles, but they tend to deteriorate significantly due to inadequate interactions with LiPS during long-term cycling [17]. Therefore, it is necessary to consider chemical interactions and adsorption through the formation of chemical bonds between LiPS and metal oxides to effectively trap the LiPS. So far, different varieties of porous heterostructures have been investigated for LSBs using strategies involving template removal (both hard and soft) and complex multiway preparation methods [18]. Zhang and coworkers utilized a template-based approach to develop TiO_2/porous carbon composites, which delivered a specific capacity of 708 mA h g^{-1} even after 150 continuous galvanostatic charge–discharge (GCD) cycles [19].

Further, it is important for an ideal interlayer material to hold polar or hydrophilic characteristics. Several metal oxides such as ZnO [20], MnO_2 [21], V_2O_5 [22], TiO_2 [19], cobalt oxide (Co_3O_4) [23], tin di-oxide (SnO_2) [24], and iron oxide (Fe_2O_3) [23], as well as their lower oxidation state oxides with specific structures, were utilized for LiPS confinement [25, 26]. Among these metal oxides, SnO_2 shows interesting electrochemical performance due to its competitive semiconducting properties, mechanical rigidity, chemical stability, environmental friendliness, and abundance [14]. The polar or hydrophilic characteristics of SnO_2 are expected to enable strong chemical bonding with LiPS, thereby limiting its diffusion. Spray drying is a well-established technique that is used to prepare metal oxides such as nickel oxide (NiO), Co_3O_4, SnO_2, copper oxide (CuO), molybdenum oxide (MoO_3), Fe_2O_3, zinc manganite ($ZnMn_2O_4$), nickel molybdate ($NiMoO_4$), and nikckel vanadate ($Ni_3V_2O_8$), etc. [27–29]. By considering its cost-effectiveness and ease of preparation, spray drying is commonly utilized to produce porous metal oxide microspheres [27, 30]. However, the facile synthesis and application of macroporous microspheres combined with a carbonaceous material have not yet been reported for LSBs. Additionally, the innovation of this study lies in its use of spray drying to create a highly porous and conductive interlayer, which not only addresses the common issues of volume expansion and poor conductivity in LSBs but also enhances Li–ion diffusion and charge transfer processes.

Herein, a comprehensive investigation of the morphology and electrochemical properties of PCMs embedded with SnO_2 quantum dots (QDs) within a carbon skeleton, referred to as "P-SnO_2@PCMs," and exploited as a multipurpose interlayer for LSBs, is performed. Microsphere morphology was achieved using a scalable spray drying process while ordered macropores were generated via polystyrene (PS) nanobeads degradation. The porous nature of P-SnO_2@PCMs microspheres ensures efficient penetration of electrolytes and mitigates undesirable volume changes during electrochemical activities. The porous carbon framework enhances the electronic conductivity and provides multiple conductive pathways, enabling rapid charge transfer, which facilitates redox reactions. Furthermore, SnO_2 QDs behave like dynamic sites for coherent capturing and conversion of polysulfide molecules through electrocatalysis. To utilize P-SnO_2@PCMs microspheres as a functional interlayer, they were applied on the cathode side of a polypropylene separator. Through experimental findings, it is demonstrated that employing P-SnO_2@PCMs microspheres as a functional interlayer in Li–S cells leads to improved electrochemical performance, which includes enhanced Li–ion diffusion, stable cycling, and rate capability. This innovative approach not only addresses the long-standing issues in LSB technology but also provides a scalable and practical solution for enhancing battery performance. The outcomes of this study are expected to significantly impact the development of high-performance, durable LSBs, making a substantial contribution to the energy storage industry. By refining the synthesis and application of P-SnO_2@PCMs, this research opens new possibilities for the advance of next-generation storage systems. Therefore, the inclusive analysis of the microstructural and electrochemical properties summarized in this study provides valuable perceptions for the improvement of porous and conductive heterostructures as multifunctional interlayers for metal–sulfur battery fields.

2. Material and Method

2.1. Sample Synthesis. The PCMs embedded with SnO_2 QDs within carbon skeleton (P-SnO_2@PCMs) microspheres were prepared using a spray drying technique followed by oxidation. The spray drying setup described in Scheme S1 was utilized to produce spherical microspheres. The solution used for spray drying was prepared using 1.5 g of dextrin hydrate [$(C_6H_{10}O_5)_n.nH_2O$, DAEJUNG, Extra pure] and 1.5 g of tin (IV) chloride pentahydrate ($SnCl_4{\cdot}5H_2O$, SAMCHUN, 98.0%) in 20 mL of deionized (DI) water via ultrasonication for 1 h. Afterward, 10 mL of PS nanobead suspension ($\phi = 150$ nm) with a concentration of 0.1 g mL^{-1} was added to the solution mentioned above while stirring continuously. The PS nanobeads suspension was prepared using a previously reported method

[31]. After stirring vigorously, the homogeneous solution was atomized at a pressure of 0.2 bar and then passed through a two-fluid nozzle. The outlet and inlet temperatures during spray drying were optimized at 100°C and 190°C, respectively. The resultant as-sprayed microspheres were transferred to a box furnace and heated in an air atmosphere. The heating step involved ramping up the temperature to 300°C at 5°C min^{-1} and hold for a duration of 3 h. For comparison, filled carbon microspheres (referred to as "FCMs") were also prepared using the previously reported Stöber method [32]. In detail, 1.4 g of resorcinol and 1.0 mL of 25–30 wt% ammonia water were dissolved in 20 mL of DI water to get the solution A. Similarly, 0.7 g of 35 wt% formaldehyde was dispersed in 20 mL of DI water to achieve solution B. Solution A and solution B were transferred to 40 mL of DI water simultaneously and then stirred overnight to form resorcinol formaldehyde (RF) precursor solution. Further, the RF solution was transferred to an autoclave and heated for 24 h at 100°C, followed by natural cooling. The resultant solid powders were centrifuged, washed multiple times with DI water and ethanol to remove excess solvent and impurities, and finally dried in an oven at 60°C to get the RF-24 precursor. The RF-24 precursor was then carbonized through a heating process at 700°C for 5 h in a nitrogen (N_2) atmosphere to obtain the FCMs.

2.2. Physical Characterization. The morphology and microstructural investigation of P-SnO_2@PCMs and FCMs were performed using field-emission transmission electron microscopy (FE-TEM, JEOL, JEM-2100F) at the Korea Basic Science Institute (Daegu) and field-emission scanning electron microscopy (FE-SEM, ULTRA PLUS, ZEISS). X-ray diffraction (XRD, D2 PHASER, Bruker) was employed to confirm the crystallinity of samples. The chemical states and electronic structure of the samples were investigated using X-ray photoelectron spectroscopy (XPS, K-Alpha, Thermo Fisher Scientific) with microfocus monochromated Al Kα X-rays. Thermogravimetric analysis (TGA) was operated on a TGA Q50 system (TA INSTRUMENTS) under an air atmosphere with a ramping rate of 10°C min^{-1} and a temperature range of 25–800°C. The porous nature, pore size distribution, and surface area of the samples were examined using the BET (Brunauer–Emmett–Teller) and BJH (Barrett–Joyner–Halenda) methods through N_2 adsorption–desorption isotherm measurements.

2.3. Coin-Cell Fabrication and Redox Performance. The P-SnO_2@PCMs microspheres were exploited as a multipurpose interlayer using a slurry casting method. The interlayer was prepared by mixing P-SnO_2@PCMs microspheres, conductive carbon black, and polyvinylidene difluoride (PVDF) binder with a mass ratio of 7:2:1, respectively, and stirred overnight in the solvent of N-methyl-2-pyrrolidone (NMP). The obtained homogeneous slurry was coated on a commercial celgard separator and thereby dried overnight at 60°C in an oven. The coated separator was punched into circular disks of 19 mm diameter. Likewise, sulfur (S) cathodes were prepared through a process that involves the homogenous mixing of elemental S, carbon black, and PVDF in the mass ratio of 7:2:1 with the help of NMP. This mixture was coated on aluminum foil and subsequently dried overnight at 60°C to eliminate the NMP solvent. The dried S cathode was pressed into circular disks of 14 mm diameter (S-loading ~1.73 mg cm^{-2}). After the completion of drying, the coated separator and S electrode were transferred to an Ar-filled glove box (with H_2O and O_2 levels $\leq$0.5 ppm). CR2032 coin cells consisting of S electrode, Li metal, and the coated separator as positive, negative, and multipurpose interlayer, respectively, were fabricated. The electrolyte comprised a blend of 1,2-dimethoxyethane (DME) and 1,3-dioxolane (DOL) present in 1:1 (by volume) and 1.0 mol L^{-1} lithium bis-(trifluoromethanesulfonyl) imide as salt. Additionally, 0.5 mol L^{-1} $LiNO_3$ was introduced into the mixture as an additive. For better comparison, Li–S cells utilizing interlayer coated with FCMs were also assembled. The amount of electrolyte was fixed at 20 µL mg^{-1}. A WBCS3000 battery cycler (WonATech) was used to measure all the electrochemical results within the voltage range of 1.7–2.8 V at room temperature. Cyclic voltammetry (CV) test results were studied at the scan rate of 0.1 mV s^{-1}. The assembled cells were cycled at different current rates ranging from 0.1 to 2.0 C, with the C-rate corresponding to 1675 mA h g^{-1}. Galvanostatic intermittent titration technique (GITT) measurement was conducted at a constant current density of 0.1 C for 10 min, tailed by a resting time of 1 h.

3. Results and Discussion

The detailed formation mechanism of uniformly ordered macroporous microspheres, referred to as P-SnO_2@PCMs, consisting of SnO_2 QDs embedded in a conductive carbon matrix, is presented. The process involves a feasible spray drying followed by heating at 300°C for 3 h, as illustrated in Scheme 1. In the initial step (Scheme 1—①), the atomizer generates spherical droplets containing a well-dispersed mixture of Sn salt, PS nanobeads ($\phi = 150$ nm), and dextrin. The collected powder from the spray drying process shows a highly compact form (Scheme 1—②). Next, the powder consisting of the composite of Sn salt, dextrin, and PS nanobeads undergoes heat treatment in the presence of an air atmosphere at 300°C for 3 h. The heat treatment results in the conversion of the tin chloride precursor into tin dioxide, while the thermal degradation of PS nanobeads generates equivalently distributed macropores within the microspheres (Scheme 1—③). Likewise, dextrin undergoes a transformation into amorphous carbonaceous products [33], efficiently prevents the agglomeration and crystal growth of SnO_2 QDs. Therefore, uniformly ordered macroporous microspheres are formed, consisting of equivalently distributed SnO_2 QDs embedded within a carbon framework, as shown in Scheme 1.

The validation of this formation mechanism is verified through microstructural characterizations of the prepared powder. The microstructural and XRD analysis of the porous microspheres obtained after the spray drying process are shown in Figure 1. Figure 1a,b presents low- and high-magnification FE-SEM images, respectively, revealing the successful synthesis of nonagglomerated microspheres ($\varphi = 2.5$ µm). Further, the FE-TEM image displayed in Figure 1c confirms the presence

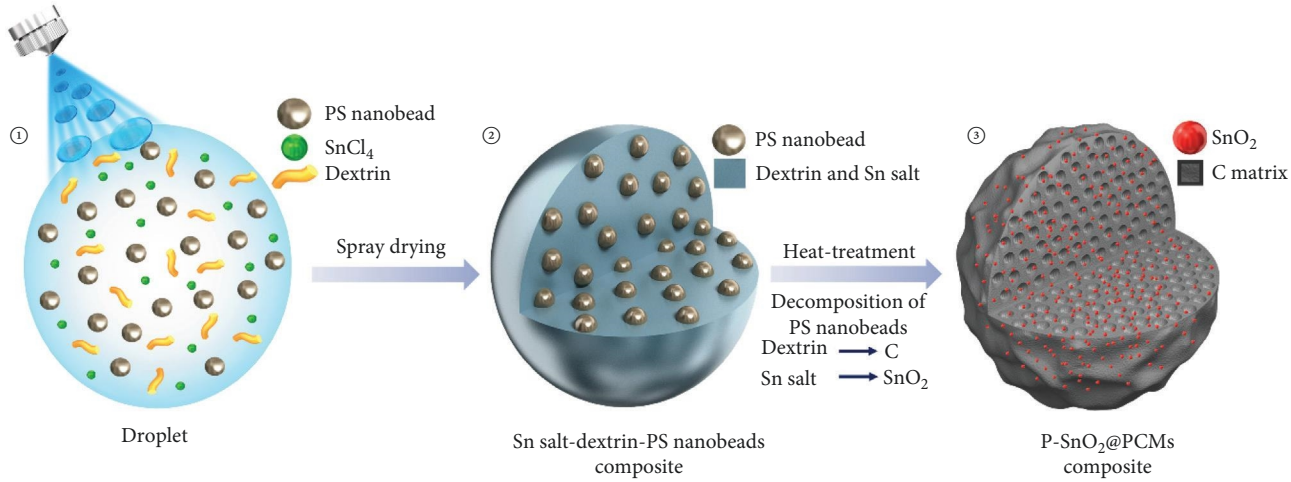

Scheme 1: Graphic representation (①, ②, and ③) of P-SnO_2@PCMs nanostructures formation prepared by spray drying technique and subsequent heating process.

of uniformly distributed PS nanobeads (i.e., pore generators) within the interior of the microspheres along with the dextrin composited amorphous-like SnO_x. The presence of multiple tin oxide phases with low crystallite size is confirmed through XRD spectra in Figure 1d [34, 35]. Additionally, the existence of dextrin in the composite microspheres is confirmed by the broad hump at $2\theta = 17.6°$ [36]. Elemental mapping results shown in Figure 1e display the equivalent distribution of Sn, O, and C elements within the as-prepared composite microspheres. This proves that the microspheres as a precursor of P-SnO_2@PCMs containing uniformly distributed SnO_x crystals in the dextrin-derived matrix are obtained through the spray drying process.

The Sn salt-dextrin-PS nanobeads composite microspheres are postheat treated in an air atmosphere to obtain the final product, i.e., P-SnO_2@PCMs. The morphological and crystallographic properties of the P-SnO_2@PCMs microspheres are presented in Figure 2. The low-magnification FE-SEM image shown in Figure 2a clearly reveals nonagglomerated P-SnO_2@PCMs ($\varphi = 2.3\,\mu m$) microspheres. The observed nonagglomerated microspheres are crucial for maintaining the high surface area and ensuring uniform distribution of SnO_2 QDs, which are essential for effective polysulfide adsorption and transformation. Moreover, well-distributed interconnected macropores are evident within the interior, as further illustrated in Figure 2b and in the cross-section (inset). Additionally, the TEM image in Figure 2c provides confirmation of multiple macropores (pore size = 59 nm). The pores generated from the PS nanobeads with 150 nm shrink during the postheat-treatment process.

The high-resolution transmission electron microscopy (HR-TEM) image shown in Figure 2d reveals that SnO_2 QDs with widths less than 5 nm are embedded inside the carbon matrixed microspheres. Additionally, well-resolved fringe spacing of 0.26 nm corresponds to the (101) lattice plane of SnO_2 was also evident [35]. The selected area electron diffraction (SAED) pattern in Figure 2e shows diffraction patterns consistent with the SnO_2 phase, which provides further confirmation of the successful formation of the SnO_2 crystal phase during the heating process. The XRD pattern presented in Figure 2f endorses the existence of broad diffraction peaks corresponding to the SnO_2 phase only which aligns well with the previous findings [34, 35]. Notably, the broad XRD peaks indicate the small crystallite size of SnO_2 QDs, which is advantageous for improving the number of chemisorption sites available for polysulfide adsorption and enhancing the overall catalytic performance.

Additionally, a peak at around $2\theta = \sim 23°$, which corresponds to the dextrin-derived amorphous carbon (AC) species, overlaps with the peak region of the SnO_2 crystal phase and cannot be distinguished [36]. The average crystallite size of SnO_2 QDs in the P-SnO_2@PCMs microspheres measured from the highly intense (110) diffraction peak using the Scherrer equation ($D = K\lambda/\beta \cos\theta$) and was found to be 4 nm, which is consistent with the TEM results (Figure 2d). TGA analysis was tested to comment on the amount and presence of carbon in the P-SnO_2@PCMs microspheres. The TGA plot shown in Figure 2g exhibits a significant weight loss between 280 and 490°C, which is attributed to the combustion of AC. This significant weight loss indicates the successful incorporation of a substantial amount of AC within the microspheres, which plays a crucial role in enhancing the electrical conductivity and providing structural stability during the charge–discharge cycles in the Li–S batteries. The AC quantity in the nanostructure was measured to be 33 wt%. Moreover, the specific surface area of P-SnO_2@PCMs microspheres is determined through N_2 adsorption and desorption isotherm analysis, as shown in Figure 2h. The moderate surface area of $32\,m^2\,g^{-1}$ can be attributed to the presence of macropores attributed to the PS decomposition and dextrin-derived AC shell throughout the composite microspheres, as shown in Figure 2b. The corresponding BJH pore size distribution plot shown in Figure 2i [30, 33, 37] reveals the presence of macropores with a maximum peak at 59 nm. These macropores not only guarantee sufficient space to assist volume fluctuations but also facilitate enough electrolyte penetration during redox activities. Furthermore, the elemental dot mapping results presented in

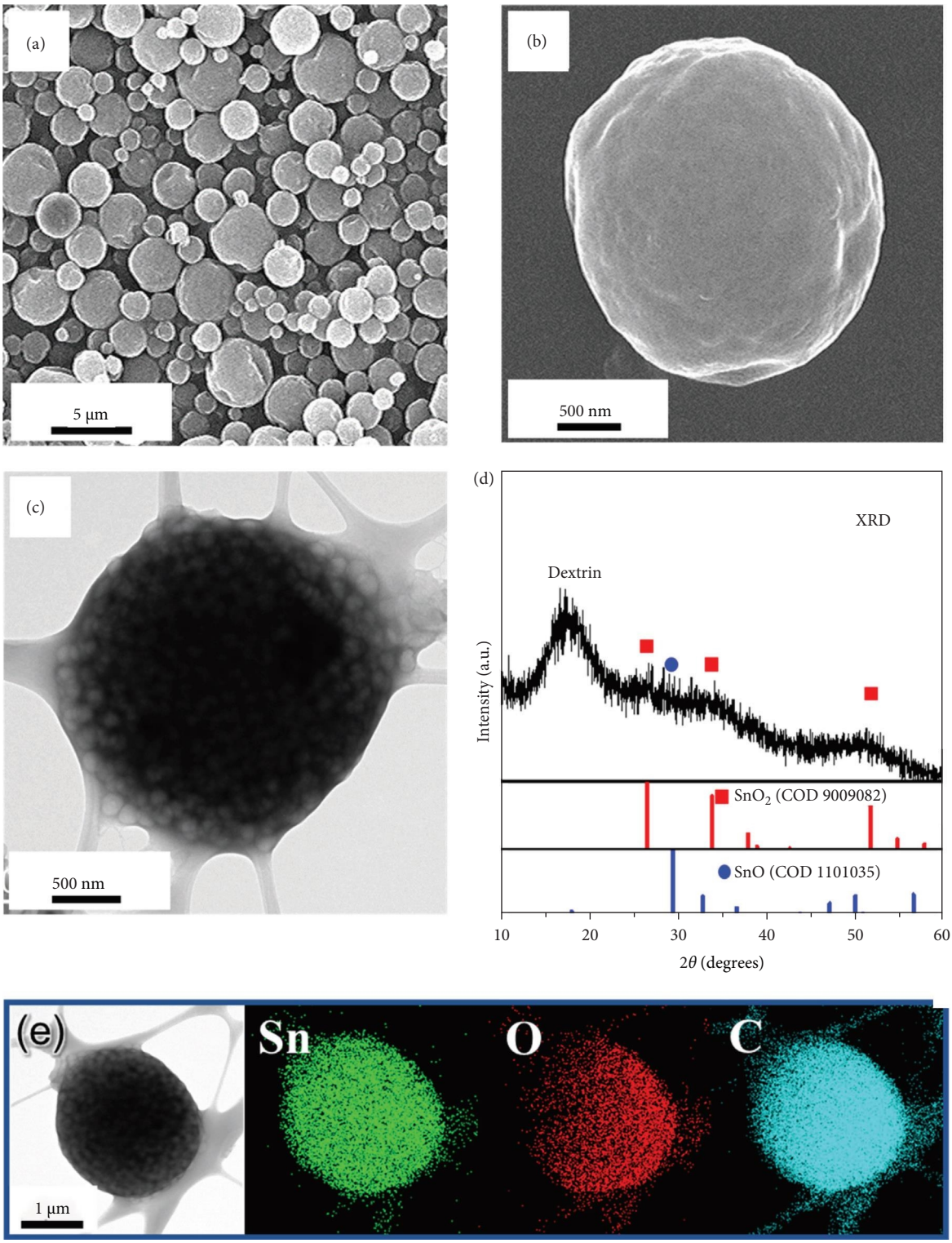

FIGURE 1: Characterization of Sn salt-dextrin-PS nanobeads composite microspheres obtained via spray-drying: (a, b) FE-SEM images, (c) TEM image, (d) XRD pattern, and (e) element mapping images. FE-SEM, field-emission scanning electron microscopy; PS, polystyrene; TEM, transmission electron microscopy; XRD, X-ray diffraction.

Figure 2j illustrate the equivalent distribution of Sn, O, and C elements within the P-SnO_2@PCMs microspheres. For comparison, RF-derived FCMs, which were prepared using the Stöber method without the presence of dextrin, PS, and Sn-salt precursor, were also investigated. The FE-SEM images shown in Figure S1a,b demonstrate a highly filled structure ($\varphi = 2.0\,\mu m$). The XRD pattern revealed in Figure S1c further endorses the formation of RF-derived AC, as evidenced by the

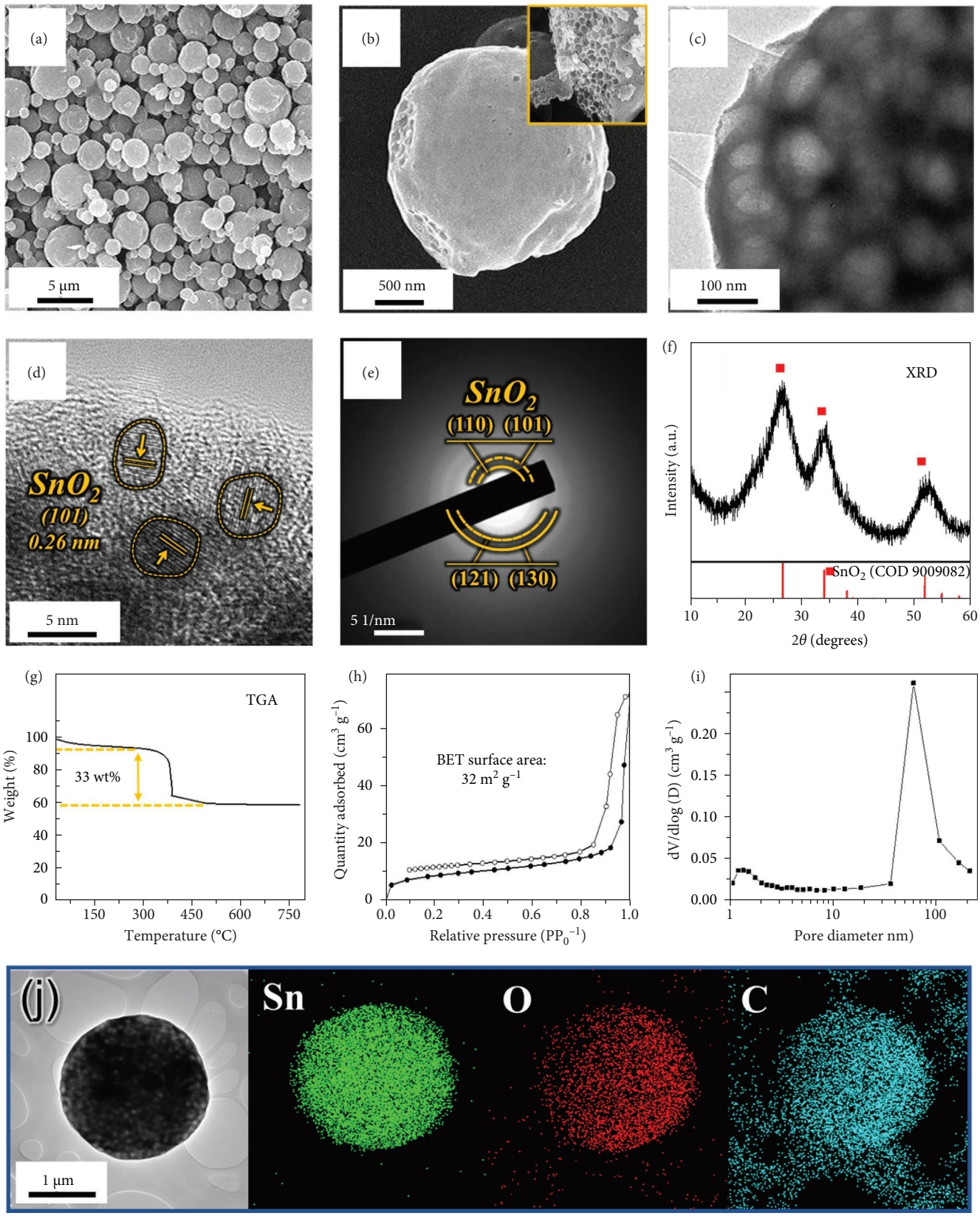

FIGURE 2: Characterization of P-SnO_2@PCMs composite microspheres obtained after oxidation at 300°C for 3 h: (a, b) FE-SEM images, (c) TEM image, (d) HR-TEM image, (e) SAED ring pattern, (f) XRD pattern, (g) TG curve in ambient atmosphere, (h) N_2 adsorption–desorption isotherms, (i) BJH pore-size distribution curve, and (j) element mapping images. BET, Brunauer–Emmett–Teller; BJH, Barrett–Joyner–Halenda; FE-SEM, field-emission scanning electron microscopy; HR-TEM, high-resolution transmission electron microscopy; SAED, selected area electron diffraction; TEM, transmission electron microscopy; TG, thermogravimetric; TGA, thermogravimetric analysis; XRD, X-ray diffraction.

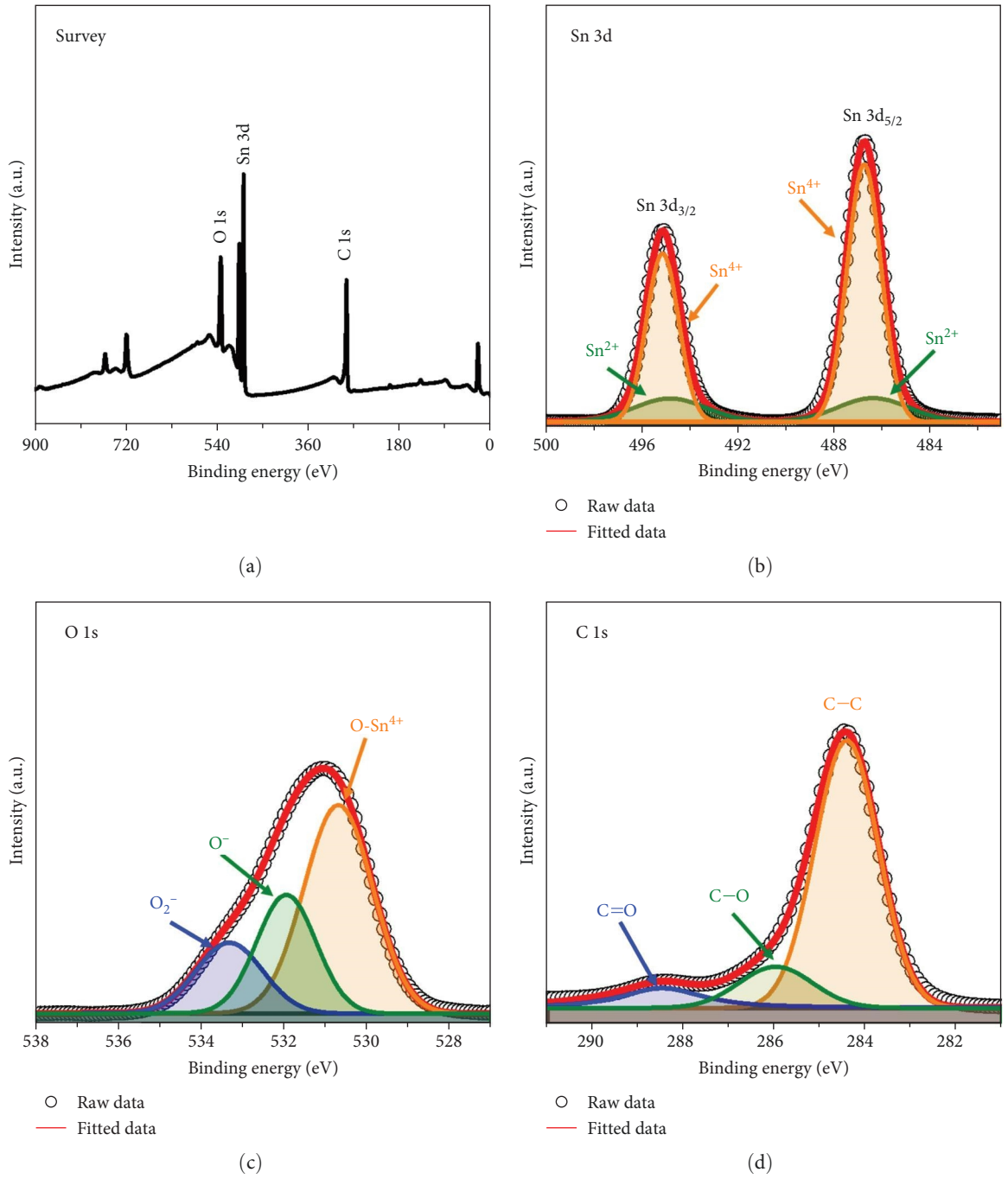

FIGURE 3: (a) XPS survey spectrum of the P-SnO_2@PCMs composite microspheres, (b) Sn 3d XPS spectrum, (c) O 1s XPS spectrum, and (d) C 1s XPS spectrum. XPS, X-ray photoelectron spectroscopy.

existence of two diffraction peaks related with the carbonaceous product [3, 38].

Furthermore, the chemical states and electronic properties of P-SnO_2@PCMs microspheres were inspected via XPS analysis. The XPS survey spectra of P-SnO_2@PCMs microspheres shown in Figure 3a reveal the presence of Sn, O, and C elements without detecting any other impurities. The high-resolution XPS spectra of Sn (3d), O (1s), and C (1s) core levels deconvoluted using Voigt curve fitting along with a Shirley background are shown in Figure 3b–d. The high-resolution XPS spectra of Sn (3d) shown in Figure 3b exhibits the spin–orbit separation of Sn $3d_{5/2}$ and Sn $3d_{3/2}$ signals located at 486.7 and 495.1 eV, respectively, which indicates the valence state of Sn^{4+} [39, 40]. Additionally, small peaks correspond to the Sn^{2+} phase are also studied [40]. The O (1s) spectra shown in Figure 3c can be separated into three distinct peaks attributed to the O-Sn^{4+} bonds (~530.7 eV), oxygen vacancy (~531.9 eV), and oxygen absorption (~533.4 eV) of the composite microspheres [41–44]. The C (1s) spectra shown in Figure 3d exhibit the peaks related to C—C, C—O, and C═O bonds at 284.5, 286.0, and 288.5 eV, respectively [42, 45]. Among

the three peaks, the C—C peak reveals the highest intensity and confirms the presence of dextrin-derived carbon species that formed during the heat treatment. Therefore, XPS data provide confirmation about the successful formation of P-SnO_2@PCMs microspheres containing a negligible amount of Sn nanodroplets, which is achieved through the spray drying process.

The performance of P-SnO_2@PCMs microspheres in LSBs was extensively investigated in this study. CV tests were executed at the voltage ramp of 0.1 mV s^{-1} for the first five cycles to study the impact of multifunctional interlayer over the redox reactions. The microspheres were uniformly coated on a Celgard separator, as shown in Figure S2, which acted as a functional interlayer. CV shape of the resulting cell with P-SnO_2@PCMs microspheres shown in Figure 4a reveals two well-defined cathodic peaks at 2.26 and 1.97 V. The distinct cathodic peaks observed in CV suggest efficient sulfur reduction processes, likely facilitated by the catalytic role of SnO_2 QDs, which enhance the conversion of polysulfides. The reduction peak at 2.26 V corresponds to the reduction of elemental sulfur to higher-order (Li_2S_x; $6 \leq x \leq 8$) and middle-order (Li_2S_x; $4 \leq x \leq 6$) polysulfide species, whereas the reduction peak at 1.97 V is attributed to further reduction to lower-order LiPSs (Li_2S_x;$1 \leq x \leq 3$) [46]. Additionally, an anodic peak at ~2.50 V indicates the efficient transformation of lower-order discharge species back into elemental sulfur through intermediate polysulfides to complete the redox cycle [47]. The CV plots for the first five cycles showed nearly overlapping behavior, which indicates the favorable Li–ion storage mechanism with P-SnO_2@PCMs-coated separator in the Li–S cells. This behavior contributed to an enhanced electrochemical performance attributed to improved ionic and electronic conduction as well as effective anchoring of polysulfides by polar SnO_2 QDs which ensures the efficient utilization of the active material. Besides, the CV plot of the cell paired with an FCMs-coated separator shown in Figure S3 exhibited less intense peaks, suggests the substandard redox activities in the cell. The charge–discharge analysis was performed at 0.1 C rate (Figure 4b) to validate the observations from the CV curves. The Li–S cell featuring P-SnO_2@PCMs interlayer exhibited a discharge capacity of 919 mA h g^{-1}, which surpasses the discharge capacity of 586 mA h g^{-1} observed in the cell coupled with FCMs-coated separator. The distinct charge–discharge plateau observed during the cycle of P-SnO_2@PCMs microspheres indicated an improved redox process involving S and Li_2S only, which corroborates the results obtained from the CV analysis. It suggests a high degree of electrochemical reversibility and efficient utilization of active material, which can be attributed to the effective polysulfide confinement and catalytic conversion by the SnO_2 QDs embedded within the carbon matrix. The high discharge capacity value for the P-SnO_2@PCMs-coated separator is due to the effective entrapment of sulfur-like products by well-confined SnO_2 QDs thereby controlling their movement towards the anode side and consequently resulted in a high proportion of active material utilization. The recorded discharge capacity value was relatively good by considering the reasonable sulfur amount on the cathode region (42 wt%). Additionally, the carbon composite microspheres provided abundant conductive pathways for the efficient transport of charged moieties, which ensures kinetically favorable redox reactions. The cells using the P-SnO_2@PCMs and FCMs-coated separator configurations were exposed to cycling experiments at 0.1 C to evaluate the longer cyclic stability, as shown in Figure 4c. The cell with P-SnO_2@PCMs functional interlayer exhibited an initial discharge capacity of 919 mA h g^{-1} (55% of the theoretical level) and decreased to 549 mA h g^{-1} after 100 cycles.

However, the capacity remained highly stable with 0.09% average capacity decay rate and reached 495 mA h g^{-1} (approximately 54% capacity retention) after 500 cycles. The stable capacity retention over 500 cycles highlights the structural integrity and catalytic activity of the P-SnO_2@PCMs interlayer, which effectively mitigates the polysulfide shuttle and preserves active material over long-term cycling. Besides, a high Coulombic efficiency of ~97% confirmed the extremely reversible reactions in the Li–S cell utilizing the P-SnO_2@PCMs-coated separator. On the other hand, the Li–S cell with FCMs-coated separator showed a similar trend but with a more pronounced capacity decay process. The initial discharge capacity was 586 mA h g^{-1} (35% of theoretical capacity), which increased to 624.7 mA h g^{-1} in 3rd cycle mainly due to the activation process. However, capacity decreases monotonically thereafter and gets stabilized at 308 mA h g^{-1} after 500 charge–discharge cycles with a 0.10% average capacity attenuation rate. The poor cycling stability of the FCMs-coated separator was credited to the lack of chemical sites in the form of SnO_2, which could effectively trap the polysulfide molecules and control the loss of active material. The electrochemical performance of multifunctional interlayers in this work is analogous to the previously available reports on various functional interlayer materials (Table S1). To further evaluate the operability of the cell under challenging conditions for Li–S cell using P-SnO_2@PCMs-coated separators, cycling performance was assessed under a high S-loading electrode (3.55 mg cm^{-2}) and a low electrolyte/sulfur ratio (10 μL mg^{-1}), as shown in Figure S4. The Li–S cell, employing the P-SnO_2@PCMs-coated separator, unveiled a first discharge capacity of 799 mA h g^{-1} (48% of theoretical capacity) at 0.1 C with an average discharge capacity retention of 61% (484 mA h g^{-1}) after 100 continuous cycles. These results strongly validate the practical applicability of P-SnO_2@PCMs-coated separators coupled with high S-loading electrodes and ultra-low electrolyte volume, ensuring fast charge diffusion and accommodating volume changes during redox reactions. To evaluate the rate performance of the Li–S cells, tests were conducted at different C-rates varying from 0.05 to 2.0 C, as shown in Figure 4d. The results reveal that Li–S cells using P-SnO_2@PCMs as multifunctional interlayers show higher initial discharge capacities compared to cells using FCMs-coated separators. At C-rates of 0.05, 0.1, 0.2, 0.3, 0.5, 0.7, 0.9, 1.0, 1.2, 1.5, 1.8, and 2.0 C, discharge capacities of 1012, 758, 669, 631, 585, 550, 511, 488, 455, 418, 366, and 321 mA h g^{-1}, respectively, were observed for Li–S cells with P-SnO_2@PCMs interlayer. This performance is attributed to the enhanced Li–ion diffusion and rapid electron transport facilitated by the porous carbon framework and catalytic SnO_2 QDs, which ensure efficient redox reactions even at higher current densities. In contrast, cells with FCMs modified separator

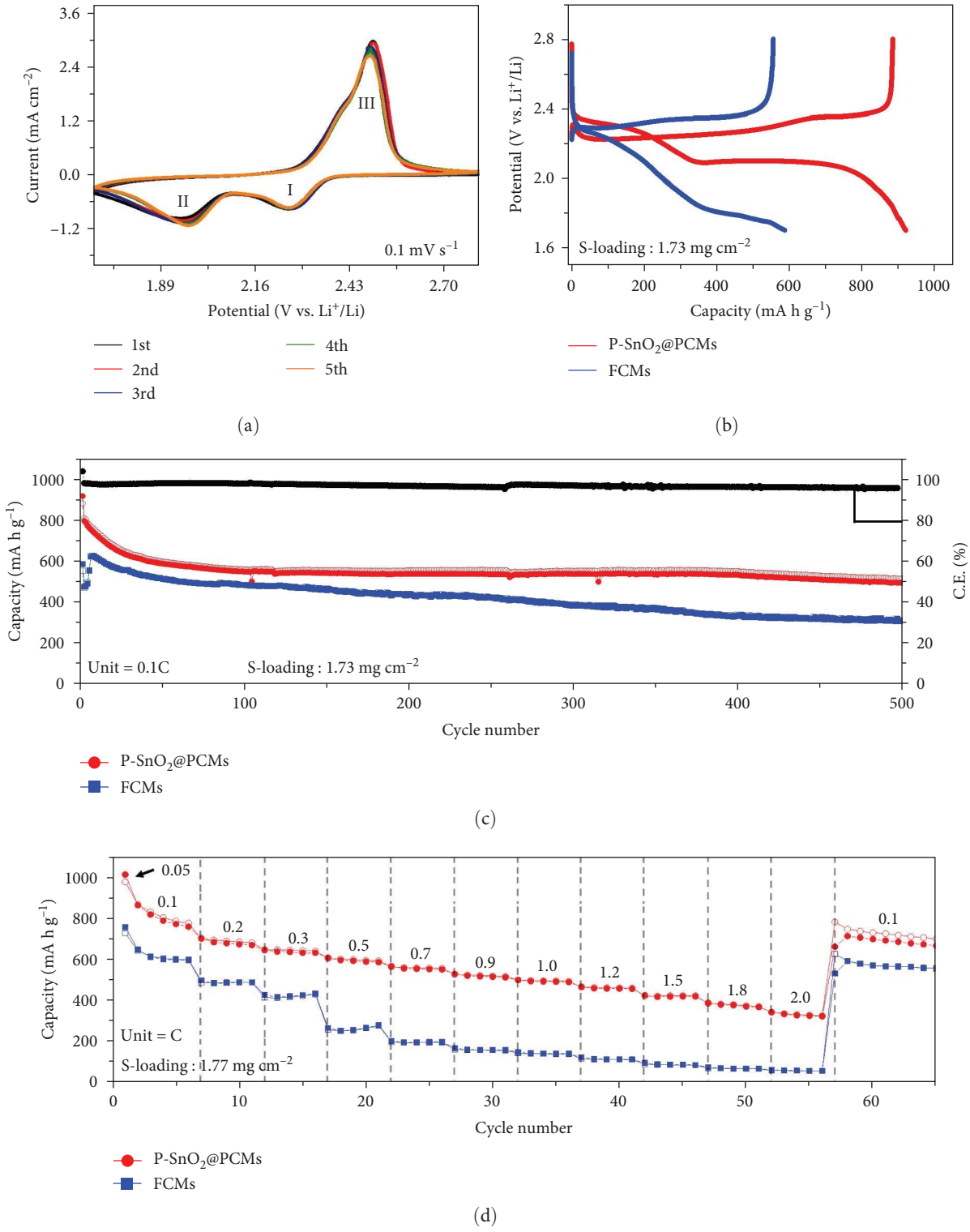

FIGURE 4: Electrochemical properties of the P-SnO$_2$@PCMs and FCMs as a functional interlayer: (a) CV plots obtained at 0.1 mV s^{-1} for first five cycles for the P-SnO$_2$@PCMs microspheres, (b) initial charge–discharge curves at 0.1 C-rate, (c) cycling performance, and (d) rate competence test at altered C-rate. CV, cyclic voltammetry; FCMs, filled carbon microspheres.

showed lower discharge capacities of 757, 595, 486, 433, 278, 197, 158, 140, 111, 85, 66, and 56 mA h g^{-1}, respectively, at identical C-rates. Notably, the discharge capacity values obtained for the P-SnO$_2$@PCMs-coated separator were significant considering the high amount of effective S on the cathode side (approximately 42 wt%). Furthermore, the cell with P-SnO$_2$@PCMs modified separator showed a capacity recovery of 642 mA h g^{-1}, corresponding to 85% of the initial

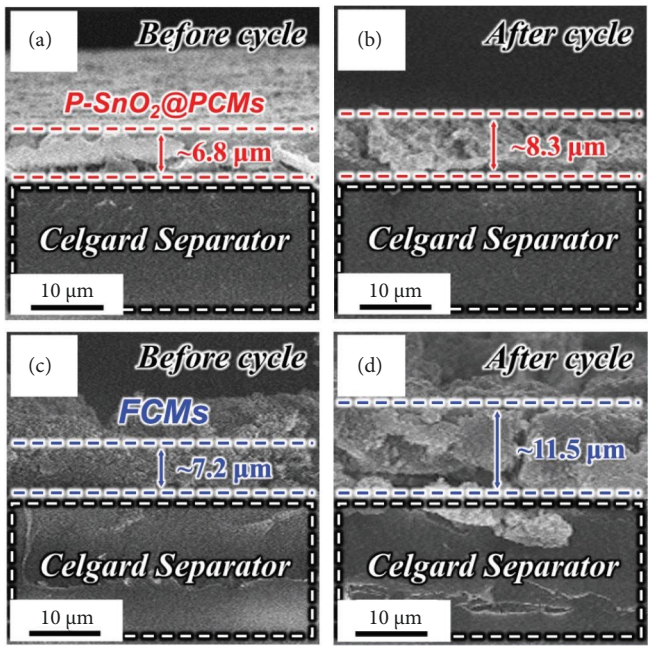

FIGURE 5: Cross-sectional FE-SEM images of the P-SnO_2@PCMs- and FCMs-coated separator; (a, c) before the cycle, (b, d) after 300th cycle at 0.1 C. FCMs, filled carbon microspheres.

capacity at 0.1 C when the current was reversed. This remarkable performance can be attributed to the highly porous heterostructure and the presence of polar species in the form of SnO_2 QDs. These structural merits ensure fast redox kinetics, efficient electrolyte infiltration, efficient capturing of polysulfide molecues and enhanced utilization of the active material. The respective charge–discharge profiles of the P-SnO_2@PCMs-coated separator (Figure S5a) exhibits long voltage plateau at different C-rates compared to the cell with FCMs-coated separator (Figure S5b), which further supports the above results. Moreover, the capacity utilization bar charts in Figure S6 also validate high active material utilization for the P-SnO_2@PCMs-coated separator compared to the FCMs-coated. To further confirm the structural advantages of P-SnO_2@PCMs, cross-sectional FE-SEM images of the functional interlayer were obtained before and after the 300th cycle at 0.1 C, as shown in Figure 5. FE-SEM image indicates that the macropores within P-SnO_2@PCMs efficiently accommodate the volume changes of those during redox reactions. For instance, the cross-sectional FE-SEM images of P-SnO_2@PCMs-coated separators before (Figure 5a) and after (Figure 5b) cycling reveals an expansion from 6.8 to 8.3 µm, which corresponds to a volume expansion of approximately 22%. In contrast, the cross-sectional FE-SEM images of the FCMs-coated separator reveal a larger expansion from 7.2 (Figure 5c) to 11.5 µm (Figure 5d), resulting in a volume change of approximately 60%. This demonstrates that the macropores within P-SnO_2@PCMs not only mitigate the volume expansion of the active material but also expedite Li^+ transport by reducing the diffusion length of charged particles. Consequently, Li–S cells employing P-SnO_2@PCMs-coated separators exhibit improved long-term cycle performance. Overall, the above results confirmed that the P-SnO_2@PCMs not only facilitate rapid redox activities by enabling proficient diffusion of charges but also effectively mitigate unwanted volume changes and efficiently trap the polysulfides, which demonstrates their structural superiority over the FCMs.

The improved reaction processes within the Li–S cell are established through Nyquist plot investigation, as presented in Figure S7a–c. The corresponding circuit fitting model and impedance values for the cell with the P-SnO_2@PCMs- and FCMs-coated separator are listed in Figure S7d,e and Table S2, respectively. The impedance values were collected for the newly fabricated cell at different stages, i.e., at open-circuit voltage and at different cycle numbers. The solution resistance (R_e) of Li–S fresh cells using P-SnO_2@PCMs- and FMCs-coated separators were measured at 6.6 and 5.8 Ω, respectively. Similarly, the charge transfer resistance (R_{ct}) was found to be 24.5 and 22.6 Ω, respectively. Even after the 100th consecutive cycle, the R_{ct} values remained consistently similar at 31.8 and 28 Ω, respectively. Notably, the cell using a P-SnO_2@PCMs-coated separator shows low charge transfer resistance (R_{ct}) during the cycling and is compared to previously reported results [4, 6, 7]. GITT measurements were conducted to further evaluate Li–ion diffusion kinetics of P-SnO_2@PCMs over FCMs despite comparable resistance values. The obtained results are presented in Figure 6. The measurements were performed at a current density of 0.1 C, with a current pulse time of 10 min and a resting time of 1 h. The equation used to calculate the Li–ion diffusion coefficient is shown below [48].

$$D_{Li^+} = \frac{4}{\pi\tau}\left(\frac{n_m V_M}{S}\right)^2\left(\frac{\Delta E_s}{\Delta E_t}\right)^2\left(\tau \ll \frac{L^2}{D_{Li^+}}\right), \quad (1)$$

where τ is the current pulse time, n_m is the mole of the sulfur, V_m is the molar volume of the sulfur, and S is the geometric area of the electrode. L is the thickness of the electrode, and ΔE_s represents the potential change after each rest time. The calculated D_{Li^+} values for P-SnO_2@PCMs and FCMs based on the given ΔE_s and ΔE_t values are 3.61×10^{-9} $cm^2\,s^{-1}$ and 8.86×10^{-10} $cm^2\,s^{-1}$, respectively. Evidently, the higher D_{Li^+} of P-SnO_2@PCMs compared to FCMs is attributed to the excellent porosity, which provides shorter diffusion paths for Li–ion along with the efficient chemical polarity induced by SnO_2 [49, 50]. Consequently, the enhanced Li–ion kinetics facilitate the rapid conversion reactions of LiPS, explaining the remarkable rate performance exhibited by P-SnO_2@PCMs.

To validate the chemical adsorption capability of the P-SnO_2@PCMs-coated separator, visual adsorption tests were conducted, as illustrated in Figure S8. The clear adsorption of LiPS was observed with the P-SnO_2@PCMs, as evidenced by a consistent color variation of the polysulfide solution from pale yellow ($T = 0$) to transparent ($T = 1$ h). Comparatively, the solution filled with FCMs exhibited poor adsorption of polysulfide mainly due to the lack of polysulfide anchoring sites, as indicated by the faintly yellowish color after 1 h. Additionally, to further validate the effective adsorption

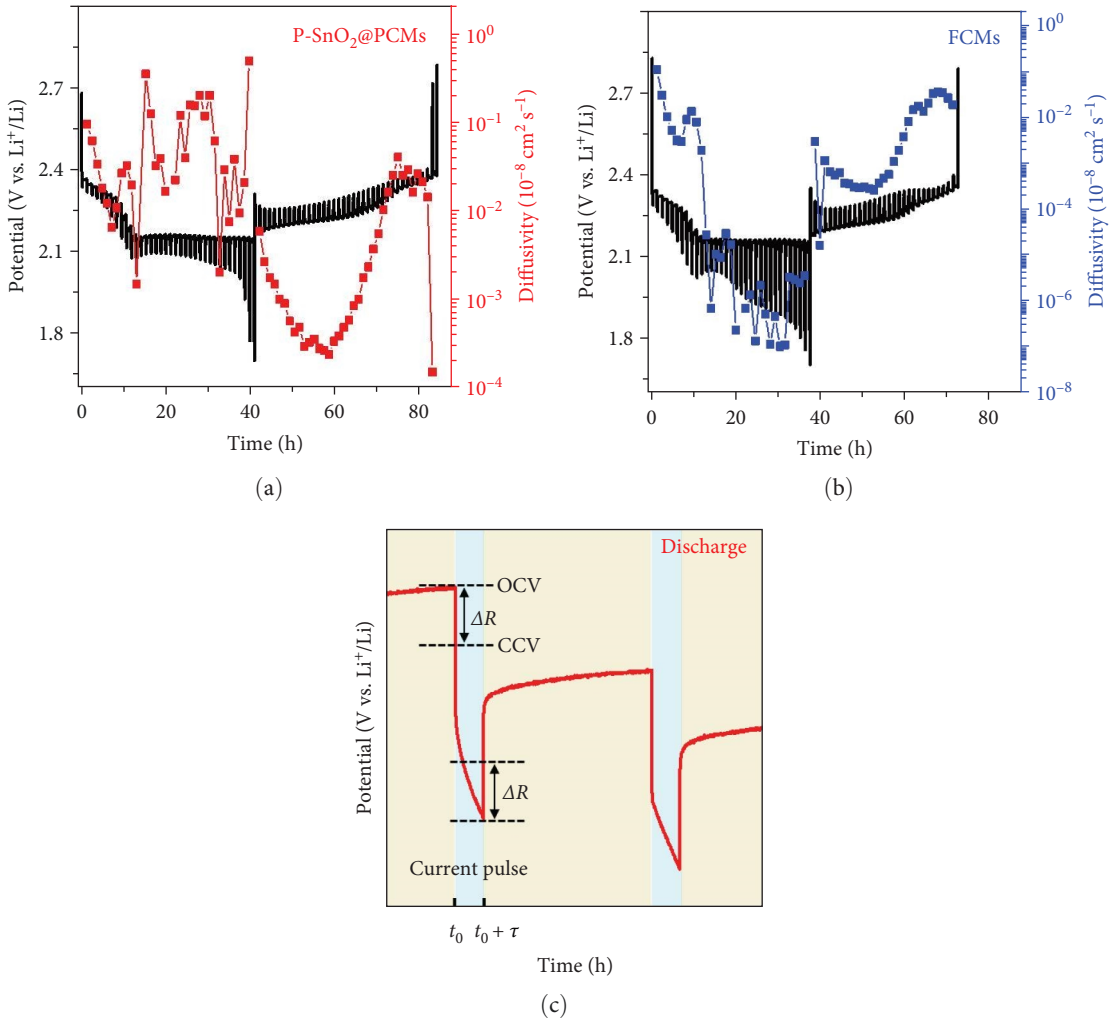

FIGURE 6: GITT curves at 0.1 C and Li–ion diffusion coefficient: (a) P-SnO_2@PCMs, (b) FCMs, and (c) schematic of the calculation of Li–ion diffusion coefficient using the GITT measurement. FCMs, filled carbon microspheres; GITT, galvanostatic intermittent titration technique.

capacity of P-SnO_2@PCMs, *ex-situ* XPS was performed using a cycled electrode to detect changes in the S 2p photoelectron signal, and the obtained results are presented in Figure S9. Notably, the two peaks that appeared at binding energies of 164.4 and 163.4 eV correspond to S $2p_{1/2}$ and S $2p_{3/2}$ spin–orbit doublet from elemental sulfur (S8), respectively [51, 52]. The clear presence of sulfur-related peaks confirms the strong chemical interaction between the SnO_2 QDs and polysulfides, effectively reducing the shuttle effect and leading to better long-term stability of the battery. Furthermore, the peak at a binding energy of 167.6 eV for both the cycled electrode is attributed to the thiosulfate ($-S_2O_3^{2-}$) groups, which originate due to surface redox reactions between polysulfides and polar materials [53]. The presence of thiosulfate species signifies the efficient conversion of higher-order soluble polysulfides to lower-order insoluble polysulfides [53]. The sharp peak at 169.2 eV corresponds to the polythionate complex formed by the reaction of S with HS^- or SO_3^{2-} species [53]. As observed, the high intensity of polythionate complex corresponding to P-SnO_2@PCMs compared to FCMs indicates better performance in inhibiting polysulfides shuttling. Finally, the peak at 170.4 eV is attributed to the sulfate ($-SO_4^{2-}$) group resulting from LiTFSI decomposition within the Li–S cell and is designated as Li_xSO_y species [54]. These results verify that the structural advantage in P-SnO_2@PCMs effectively immobilizes polysulfide species through the embedded SnO_2 QDs within PCMs and enhances the active material usage, which resulted in superior electrochemical properties. These results confirm that the P-SnO_2@PCMs-coated separator shows the maximum sulfur utilization at all C-rates, demonstrating the rapid redox reaction compared to FCMs-coated separator at high current densities. Therefore, the structural benefits in P-SnO_2@PCMs microspheres offers synchronized effects on improving the overall electrochemical performance of the Li–S cell.

4. Conclusions

In summary, this work layout an innovative functional interlayer to achieve stable Li–S battery performance. This interlayer comprises ordered macroporous microspheres embedded with SnO_2 QDs within a conductive carbon skeleton (P-SnO_2@PCMs). The porous nature of the composite microspheres ensures efficient

penetration of the electrolyte, shortens the diffusion distance for charged moieties, and accommodates severe volume changes. Furthermore, the porous carbon framework significantly boosts the overall conductivity of the heterostructures by initiating multiple conductive pathways for rapid electron transfer, thus promoting favorable redox reactions. The existence of polar SnO_2 QDs within the interlayer serves as chemisorption sites which facilitates effective confinement and electrocatalytic transformation of polysulfide and other sulfur-like products. Li–S cells incorporating the P-SnO_2@PCMs-coated separator as the functional interlayer demonstrate an outstanding rate capability up to 2.0 C and exhibit excellent cycling stability at 0.1 C rate. These enhancements in electrochemical performance can be attributed to the immediate charge transfer, rapid dissemination of charged moieties, and effective capturing of polysulfide species, which result in enhanced utilization of the active material. This work successfully addresses several key challenges in LSB development, offering a more integrated approach that enhances both the physical and chemical stability of the battery system. These findings lay the groundwork for further refinement and optimization in future studies.

Data Availability Statement

The data used to support the findings of this study are included within the article.

Conflicts of Interest

The authors declare no conflicts of interest.

Author Contributions

Kun Woo Baek designed the idea, carried out experiments, and prepared the primary blueprint. Geon Hui Oh executed experiments and data accumulation. Rakesh Saroha was responsible for writing–review. Dong-Won Kang was responsible for supervision and review. Gi Dae Park was responsible for supervision. Jung Sang Cho was responsible for supervision and writing–review and editing. Kun Woo Baek and Geon Hui Oh contributed equally to this work.

Funding

This work was supported by the National Research Foundation of Korea (NRF) and the Commercialization Promotion Agency for R&D Outcomes (COMPA) funded by the Ministry of Science and ICT (Grant No.: RS-2023-00217581, RS-2023-00304768).

Supporting Information

Additional supporting information can be found online in the Supporting Information section. (*Supporting Information*) Additional figures showing the schematic diagram of the spray drying system, FE-SEM and XRD of RF-derived filled carbon microspheres, digital photograph of the P-SnO_2@PCMs microsphere, cyclic voltammetry for FCMs coated-separator, comparison table, charge-discharge curves for Li–S cells employing different coated-separators, capacity utilization bar chart, EIS spectra with P-SnO2@PCMs- and FCMs-coated separator, equivalent circuit fitting model, EIS parameters comparison table, digital photographs of visual demonstration, and the postcycling XPS profile. This information is available from the Wiley Online Library or from the author.

References

[1] R. Saroha, J.-H. Ahn, and J. S. Cho, "A Short Review on Dissolved Lithium Polysulfide Catholytes for Advanced Lithium-Sulfur Batteries," *Korean Journal of Chemical Engineering* 38, no. 3 (2021): 461–474.

[2] R. Monsef and M. S. Niasari, "Fundamental Understanding on Cyclability Behaviors of Ammonium Vanadate Nanoarchitectures as Cathode Materials for Li-Ion Batteries: A Comparative Insight of Dual Modification of Precursor and Morphology," *Journal of Energy Storage* 74 (2023): 109395.

[3] R. Saroha and J. S. Cho, "Nanofibers Comprising Interconnected Chain-Like Hollow N-Doped C Nanocages as 3D Free-Standing Cathodes for Li-S Batteries With Super-High Sulfur Content and Lean Electrolyte/Sulfur Ratio," *Small Methods* 6, no. 5 (2022): 2200049.

[4] X. Yang, Z. Ran, F. Luo, Y. Li, P. Zhang, and H. Mi, "Free-Standing ZIF-8 Derived Nitrogen and Sulfur Co-Doped Porous Carbon Nanofibers Host for High Mass Loading Lithium-Sulfur Battery," *Applied Surface Science* 509 (2020): 145270.

[5] J. M. Choi, R. Saroha, J. S. Kim, M. R. Jang, and J. S. Cho, "Porous Nanofibers Comprising VN Nanodots and Densified N-Doped CNTs as Redox-Active Interlayers for Li-S Batteries," *Journal of Power Sources* 559 (2023): 232632.

[6] R. Saroha, Y. H. Seon, B. Jin, et al., "Self-Supported Hierarchically Porous 3D Carbon Nanofiber Network Comprising Ni/Co/$NiCo_2O_4$ Nanocrystals and Hollow N-Doped C Nanocages as Sulfur Host for Highly Reversible Li-S Batteries," *Chemical Engineering Journal* 446 (2022): 137141.

[7] R. Saroha, J. H. Oh, Y. H. Seon, et al., "Freestanding Interlayers for Li-S Batteries: Design and Synthesis of Hierarchically Porous N-Doped C Nanofibers Comprising Vanadium Nitride Quantum Dots and MOF-Derived Hollow N-Doped C Nanocages," *Journal of Materials Chemistry A* 9, no. 19 (2021): 11651–11664.

[8] R. Saroha, J. Heo, Y. Liu, et al., "V_2O_3-Decorated Carbon Nanofibers as a Robust Interlayer for Long-Lived, High-Performance, Room-Temperature Sodium-Sulfur Batteries," *Chemical Engineering Journal* 431 (2022): 134205.

[9] C. Deng, Z. W. Wang, S. P. Wang, and J. X. Yu, "Inhibition of Polysulfide Diffusion in Lithium-Sulfur Batteries: Mechanism and Improvement Strategies," *Journal of Materials Chemistry A* 7, no. 20 (2019): 12381–12413.

[10] W. C. Ren, W. Ma, S. Zhang, and B. T. Tang, "Recent Advances in Shuttle Effect Inhibition for Lithium Sulfur Batteries," *Energy Storage Materials* 23 (2019): 707–732.

[11] B. Moorthy, S. H. Kwon, J. H. Kim, P. Ragupathy, H. M. Lee, and D. K. Kim, "Tin Sulfide Modified Separator as an Efficient Polysulfide Trapper for Stable Cycling Performance in Li-S Batteries," *Nanoscale Horizons* 4, no. 1 (2019): 214–222.

[12] Y. S. Su and A. Manthiram, "Lithium-Sulphur Batteries With a Microporous Carbon Paper as a Bifunctional Interlayer," *Nature Communications* 3 (2012): 1166.

[13] A. Raulo, S. Singh, A. Gupta, R. Srivastava, and B. Nandan, "Metal Oxide Heterostructure Decorated Carbon Nanofiber as

a Novel Redox Catalyst for High Performance Lithium-Sulfur Batteries," *Applied Surface Science* 569 (2021): 151054.

[14] N. Hu, X. S. Lv, Y. Dai, L. L. Fan, D. B. Xiong, and X. F. Li, "SnO_2/Reduced Graphene Oxide Interlayer Mitigating the Shuttle Effect of Li-S Batteries," *ACS Applied Materials & Interfaces* 10, no. 22 (2018): 18665–18674.

[15] R. T. Guo, W. Li, R. Q. Huang, M. Q. Chen, Z. Lie, and G. C. Han, "Shuttle-Inhibited 3D Sandwich MXene/SnO_2 QDs Sulfur Host for High-Performance Lithium-Sulfur Batteries," *Journal of Alloys and Compounds* 937 (2023): 168427.

[16] Z. Li, C. Y. Qi, Q. Chang, J. Jin, Y. Lu, and Z. Y. Wen, "TiC Nanoparticles Supported on Free-Standing Carbon Nanofibers Enabled High-Performance Lithium-Sulfur Batteries," *Composites Part B: Engineering* 257 (2023): 110679.

[17] C. J. Hart, M. Cuisinier, X. Liang, D. Kundu, A. Garsuch, and L. F. Nazar, "Rational Design of Sulphur Host Materials for Li-S Batteries: Correlating Lithium Polysulphide Adsorptivity and Self-Discharge Capacity Loss," *Chemical Communications* 51, no. 12 (2015): 2308–2311.

[18] L. Wu, Z. Y. Fu, and B. L. Su, "Hierarchically Structured Porous Materials: Synthesis Strategies and Applications in Energy Storage," *National Science Review* 7, no. 11 (2020): 1667–1701.

[19] H. S. Han, S. Q. Niu, Y. Zhao, T. Z. Tan, and Y. G. Zhang, "TiO_2/Porous Carbon Composite-Decorated Separators for Lithium/Sulfur Battery," *Nanoscale Research Letters* 14 (2019): 176.

[20] R. L. Yang, H. W. Du, Z. Q. Lin, et al., "ZnO Nanoparticles Filled Tetrapod-Shaped Carbon Shell for Lithium-Sulfur Batteries," *Carbon* 141 (2019): 258–265.

[21] Y. Li, D. X. Ye, W. Liu, et al., "A MnO_2/Graphene Oxide/Multi-Walled Carbon Nanotubes-Sulfur Composite With Dual-Efficient Polysulfide Adsorption for Improving Lithium-Sulfur Batteries," *ACS Applied Materials & Interfaces* 8, no. 42 (2016): 28566–28573.

[22] C. Liu, M. Xiang, H. Y. Zhang, et al., "Preparation and Electrochemical Performance of V_2O_5@ N-CNT/S Composite Cathode Materials," *Frontiers in Energy Research* 8 (2021): 615558.

[23] P. Wang, R. Zeng, L. You, et al., "Graphene-Like Matrix Composites With Fe_2O_3 and Co_3O_4 as Cathode Materials for Lithium-Sulfur Batteries," *ACS Applied Nano Materials* 3, no. 2 (2020): 1382–1390.

[24] Q. Q. Liu, Q. Jiang, L. Jiang, et al., "Preparation of SnO_2@rGO/CNTs/S Composite and Application for Lithium-Sulfur Battery Cathode Material," *Applied Surface Science* 462 (2018): 393–398.

[25] Z. Li, J. T. Zhang, B. Y. Guan, D. Wang, L. M. Liu, and X. W. Lou, "A Sulfur Host Based on Titanium Monoxide@-carbon Hollow Spheres for Advanced Lithium-Sulfur Batteries," *Nature Communications* 7 (2016): 13065.

[26] H. Tang, S. S. Yao, S. K. Xue, et al., "In-Situ Synthesis of Carbon@Ti_4O_7 Non-Woven Fabric as a Multi-Functional Interlayer for Excellent Lithium-Sulfur Battery," *Electrochimica Acta* 263 (2018): 158–167.

[27] J. K. Kim, S. Y. Jeong, S. H. Lim, et al., "Recent Advances in Aerosol-Assisted Spray Processes for the Design and Fabrication of Nanostructured Metal Chalcogenides for Sodium-Ion Batteries," *Chemistry An Asian Journal* 14, no. 18 (2019): 3127–3140.

[28] J. S. Park, J. K. Kim, J. H. Hong, J. S. Cho, S. K. Park, and Y. C. Kang, "Advances in the Synthesis and Design of Nanostructured Materials by Aerosol Spray Processes for Efficient Energy Storage," *Nanoscale* 11, no. 41 (2019): 19012–19057.

[29] J. S. Cho and Y. C. Kang, "All-in-One Beaker Method for Large-Scale Production of Metal Oxide Hollow Nanospheres Using Nanoscale Kirkendall Diffusion," *ACS Applied Materials & Interfaces* 8, no. 6 (2016): 3800–3809.

[30] J. S. Park, J. S. Cho, and Y. C. Kang, "Scalable Synthesis of $NiMoO_4$ Microspheres With Numerous Empty Nanovoids as an Advanced Anode Material for Li-Ion Batteries," *Journal of Power Sources* 379 (2018): 278–287.

[31] M. S. Jo, S. Ghosh, S. M. Jeong, Y. C. Kang, and J. S. Cho, "Coral-Like Yolk-Shell-Structured Nickel Oxide/Carbon Composite Microspheres for High-Performance Li-Ion Storage Anodes," *Nano-Micro Letters* 11 (2019): 3.

[32] C. Y. Fan, M. Y. Ou, P. Wei, et al., "Hard Carbon Spheres Prepared by a Modified Stober Method as Anode Material for High-Performance Potassium-Ion Batteries," *RSC Advances* 11, no. 24 (2021): 14883–14890.

[33] J. S. Park, J. S. Cho, and Y. C. Kang, "Nickel Vanadate Microspheres With Numerous Nanocavities Synthesized by Spray Drying Process as an Anode Material for Li-Ion Batteries," *Journal of Alloys and Compounds* 780 (2019): 326–333.

[34] J. S. Cho and Y. C. Kang, "Nanofibers Comprising Yolk-Shell Sn@void@SnO/SnO_2 and Hollow SnO/SnO_2 and SnO_2 Nanospheres via the Kirkendall Diffusion Effect and Their Electrochemical Properties," *Small* 11, no. 36 (2015): 4673–4681.

[35] J. S. Cho, H. S. Ju, and Y. C. Kang, "Applying Nanoscale Kirkendall Diffusion for Template-Free, Kilogram-Scale Production of SnO_2 Hollow Nanospheres via Spray Drying System," *Scientific Reports* 6 (2016): 23915.

[36] A. Radoń and P. Włodarczyk, "Influence of Water on the Dielectric Properties, Electrical Conductivity and Microwave Absorption Properties of Amorphous Yellow Dextrin," *Cellulose* 26 (2019): 2987–2998.

[37] M. Amiri, M. S. Niasari, A. Akbari, and T. Gholami, "Removal of Malachite Green (a Toxic Dye) From Water by Cobalt Ferrite Silica Magnetic Nanocomposite: Herbal and Green Sol-Gel Autocombustion Synthesis," *International Journal of Hydrogen Energy* 42 (2017): 24846–24860.

[38] R. T. Penki, B. N. Munichandraiah, and D. Shanmughasundaram, "High Rate Capability of Coconut Kernel Derived Carbon as an Anode Material for Lithium-Ion Batteries," *Advanced Materials Letters* 5, no. 4 (2014): 184–190.

[39] J. H. Kim, K. M. Jeon, J. S. Park, and Y. C. Kang, "Excellent Li-Ion Storage Performances of Hierarchical SnO-SnO_2 Composite Powders and SnO Nanoplates Prepared by One-Pot Spray Pyrolysis," *Journal of Power Sources* 359 (2017): 363–370.

[40] M. Kwoka, L. Ottaviano, M. Passacantando, S. Santucci, G. Czempik, and J. Szuber, "XPS Study of the Surface Chemistry of L-CVD SnO_2 Thin Films After Oxidation," *Thin Solid Films* 490, no. 1 (2005): 36–42.

[41] N. Kitchamsetti and D. Kim, "Facile Synthesis of Hierarchical Core-Shell Heterostructured ZnO/SnO_2@$NiCo_2O_4$ Nanorod Sheet Arrays on Carbon Cloth for High Performance Quasi-Solid-State Asymmetric Supercapacitors," *Journal of Materials Research and Technology* 21 (2022): 590–603.

[42] O. H. Kwon, J. H. Oh, B. Gu, et al., "Porous SnO_2/C Nanofiber Anodes and $LiFePO_4$/C Nanofiber Cathodes With a Wrinkle Structure for Stretchable Lithium Polymer Batteries With High Electrochemical Performance," *Advanced Science* 7, no. 17 (2020): 2001358.

[43] K. Thiyagarajan and K. Sivakumar, "Oxygen Vacancy-Induced Room Temperature Ferromagnetism in Graphene-SnO_2 Nanocomposites," *Journal of Materials Science* 52 (2017): 8084–8096.

[44] S. Z. Ajabshir, M. Baladi, and M. S. Niasari, "Enhanced Visible-Light-Driven Photocatalytic Performance for Degradation of Organic Contaminants Using $PbWO_4$ Nanostructure Fabricated

by a New, Simple and Green Sonochemical Approach," *Ultrasonics Sonochemistry* 72 (2021): 105420.

[45] H. Khojasteh, M. S. Niasari, H. Safajou, and H. S. Hojaghan, "Facile Reduction of Graphene Using Urea in Solid Phase and Surface Modification by N-Doped Graphene Quantum Dots for Adsorption of Organic Dyes," *Diamond and Related Materials* 79 (2017): 133–144.

[46] R. Saroha, J. H. Oh, J. S. Lee, et al., "Hierarchically Porous Nanofibers Comprising Multiple Core-Shell Co_3O_4@graphitic Carbon Nanoparticles Grafted Within N-Doped CNTs as Functional Interlayers for Excellent Li-S Batteries," *Chemical Engineering Journal* 426 (2021): 130805.

[47] R. Saroha, J. W. Heo, X. Y. Li, et al., "Asymmetric Separator Integrated With Ferroelectric-$BaTiO_3$ and Mesoporous-CNT for the Reutilization of Soluble Polysulfide in Lithium-Sulfur Batteries," *Journal of Alloys and Compounds* 893 (2022): 162272.

[48] Y. Lu, J.-L. Qin, T. Shen, et al., "Hypercrosslinked Polymerization Enabled N-Doped Carbon Confined Fe_2O_3 Facilitating Li Polysulfides Interface Conversion for Li-S Batteries," *Advanced Energy Materials* 11 (2021): 2101780.

[49] C. Wang, M. Yuan, W. Shi, et al., "Chelation-Assisted Formation of Carbon Nanotubes Interconnected Yolk-Shell Silicon/Carbon Anodes for High-Performance Lithium-Ion Batteries," *Journal of Colloid and Interface Science* 631 (2023): 747–757.

[50] C. Long, L. Li, Y. Shan, et al., "Electrochemical Investigation of Li-Ion Diffusion and Absorbing Polysulfide of Hierarchically Structured Carbon for the Quasi-Solid Lithium-Sulfur Batteries," *Ionics* 27 (2021): 3895–3902.

[51] L. Qie, W. Chen, X. Xiong, et al., "Sulfur-Doped Carbon With Enlarged Interlayer Distance as a High-Performance Anode Material for Sodium-Ion Batteries," *Advanced Science* 2, no. 12 (2015): 1500195.

[52] H. Cai, Y. Xia, C. Dao, et al., "Ambient-Air Sulfurization Process for Cu_2ZnSnS_4 Thin Film Solar Cells: Self-Creating Inert Atmosphere Using Sulfur Vapor," *Acs Applied Energy Materials* 2 (2019): 7279–7287.

[53] X. Liang, C. Hart, Q. Pang, A. Garsuch, T. Weiss, and L. F. Nazar, "A Highly Efficient Polysulfide Mediator for Lithium-Sulfur Batteries," *Nature Communications* 6 (2015): 5628.

[54] V. Sharova, A. Moretti, T. Diemant, A. Varzi, R. J. Behm, and S. Passerini, "Comparative Study of Imide-Based Li Salts as Electrolyte Additives for Li-Ion Batteries," *Journal of Power Sources* 375 (2018): 43–52.